Project acronym:	Lasers4MaaS
Project title:	Laser-as-a-Service Digital Platform with Dynamic Beam Shaping for Acceleration of Smart, Decentralised and Sustainable Factory of the Future
Call	HORIZON-CL4-2024-TWIN-TRANSITION-01-03 Manufacturing-as-Service: technologies for customised, flexible, and decentralised production on demand
Grant agreement No:	101178719
Work-package 9:	Development of full order models for physics-based digital twins
Deliverable D9.1:	High-fidelity physics-based simulation model and approaches for interoperability of digital twins
Owner:	TUW
Due date:	31/05/2026

Type		
R	Document, report (excluding the periodic and final reports)	x
DEM	Demonstrator, pilot, prototype, plan designs	
DEC	Websites, patents filling, press & media actions, videos, etc.	
DATA	Data sets, microdata, etc.	
DMP	Data management plan	
ETHICS	Deliverables related to ethics issues	
SECURITY	Deliverable related to security issues	
OTHER	Software, technical diagram, algorithms, models, etc.	

Dissemination level		
PU	Public, fully open, e.g. project website	x
SEN	Sensitive, limited under the conditions of the Grant Agreement	
Classified R-UE/EU-R	EU RESTRICTED under the Commission Decision No2015/444	

Disclaimers: this project has received funding from the European Union's HORIZON EUROPE research and innovation programme under grant agreement No. 101178719. The content of this publication is the sole responsibility of the Consortium partners listed herein and does not necessarily represent the view of the European Commission or its services.

HISTORY OF CHANGES

Version	Publication date	Change
1.1	23/04/2025	First draft
1.2	18/05/2025	Addition of data interoperability
2.0	20/05/2025	Final version

LIST OF AUTHORS

Name	Organization	Email
Tobias Florian	TUW	tobias.florian@tuwien.ac.at
Jakob David Neuhauser	TUW	jakob.neuhauser@tuwien.ac.at
Laszlo Vörös	TUW	laszlo.voeroes@tuwien.ac.at
Michael Sawannia	USTUTT	michael.sawannia@ifsw.uni-stuttgart.de

REVIEWED BY

Name	Organization	Email
Pasquale Franciosa	WMG	p.franciosa@warwick.ac.uk

TABLE OF CONTENT

1. Executive summary 8
2. Introduction 9
2.1. Background and Motivation 9
2.2. Scope of Deliverable 9
2.3. Relation to Other Work Packages and Deliverables 10
3. High-Fidelity Physics-Based Simulation Model (T9.1) 11
3.1. Model Architecture and Governing Equations 11
3.2. Extensions and updates to the existing model 12
3.3. Laser Beam Representation 13
3.4. Material Modelling for Use Cases 14
4. Calibration and Validation (T9.2) 15
4.1. Calibration Strategy 15
4.2. Benchmark Experiments 15
4.3. Validation Results 16
4.4. Identified Limitations and Uncertainty Quantifications 19
5. Reduced-Order Model Methodology Review and Selection (T9.3) 20
5.1. Requirements for ROMs Within Lasers4MaaS 20
5.2. Review and Assessment of ROM Approaches 21
5.3. Selected ROM Strategy and Justification 22
5.4. Preliminary Evidence 23
6. Interoperability of the High-Fidelity Simulations 26
7. Contribution to Project KPIs and Expected Outcomes 27
8. Summary and Conclusion 28
9. Bibliography 29

LIST OF FIGURES

Figure 1: Dynamic mesh refinement used in the simulations with fine cells applied in the regions of interest 13
Figure 2: Surface camera images compared with simulations in stainless steel (top) and aluminium (bottom) 15
Figure 3: Cross section comparison of the welding of stainless steel at a power of 5 kW and a feed rate of 0.25 m/s with two different beam shapes. The scale applies for both the cross sections and the beam shapes. [2] 17
Figure 4: Long section comparison of the welding of stainless steel at a power of 5 kW and a feed rate of 0.25 m/s with two different beam shapes (top: single spot, bottom: circle). [2] 17
Figure 5: Cross section comparison of the welding of aluminium at a power of 6 kW and a feed rate of 0.1 m/s with two different beam shapes. The scale applies for both the cross sections and the beam shapes. 18
Figure 6: Long section comparison of the welding of aluminium at a power of 6 kW and a feed rate of 0.1 m/s with two different beam shapes (top: single spot, bottom: four spots). 18
Figure 8: Examples of normalised intensity distributions of the used beam shapes. To the left is a circle with radius 0 (single spot). The middle and right figures depict circles with radii of 8 (medium circle) and 16 (large circle), respectively. 23
Figure 9: Evaluation of predictions in the forward direction. The comparison includes a Neural Network (NN), Gaussian Process Regression (GPR), and Support Vector Regression (SVR) for predicting maximum depth, length (at 50% depth), and width (at 50% depth and 50% length) from the three input parameters (power, velocity, and beam shape radius). Panels show standardised absolute error, residual variance ($1-R^2$), and relative error. Green boxes highlight the best-performing method per category. Top numerical values indicate baseline performance when always predicting the median value. 23
Figure 10: Evolution of the Median Relative Error (MedRE) with sample size when predicting output parameters using Gaussian Process Regression. 24
Figure 11: Longitudinal section of the weld pool for different shape radii as produced by the Neural Network approach. 24
Figure 12: Two-dimensional loss surface as created by the forward model for a target depth of 3 mm. While the laser power and the shape radius were varied, the welding speed was fixed at 0.25 m/s. 25
Figure 13: Power modulation and the corresponding long sections of welding simulations showing temperature and velocity fields. White color indicates the melt pool, black color indicates the resolidified material. 26

LIST OF TABLES

Table 1: Presentation of connections to other parts of the Lasers4MaaS project. 10
Table 2: Input parameters of the welding processes used for validation 16

LIST OF ABBREVIATIONS

CBC	Coherent Beam Combining
CFD	Computational Fluid Dynamics
DBS	Dynamic Beam Shaping
FOM	Full-Order Model
GPR	Gaussian Process Regression
LBW	Laser Beam Welding
ML	Machine Learning
MoF	Mass-of-Fluid
NN	Neural Network
PINN	Physics-Informed Neural Network
ROM	Reduced-Order Model
SHAP	Shapley Additive Explanations
SVR	Support Vector Regression
WP	Work Package

1. Executive summary

Deliverable D9.1 reports the work carried out under tasks T9.1, T9.2, and T9.3 of WP9, constituting the core predictive infrastructure of the Lasers4MaaS project at the M18 milestone. Together, these tasks establish a validated, high-fidelity physics-based simulation framework, define the calibration and validation methodology against experimental benchmark data, and select the reduced-order modelling (ROM) strategy that will underpin real-time AI-driven decision-making in WP7-8 and the full ROM implementation in WP10.

Under T9.1, the existing compressible multiphase Mass-of-Fluid Full-Order Model (FOM) was further developed. The employed model is a so called two-fluid model and generates the recoil pressure effect naturally through vapor dynamics, eliminating the need for empirical recoil pressure coefficients [1]. This physically self-consistent treatment represents the primary technical innovation of the framework. The model incorporates Coherent Beam Combining (CBC) laser representations, supporting both static and dynamic beam shaping configurations, and covers two material systems: stainless steel, serving use cases UC2, UC3, and UC5, and aluminium, targeting UC1 and UC4. Post-processing routines extract welding fingerprints like depth, width, and length, and are able to export them into interoperable formats like JSON and CSV formats, with the possibility to align field naming to the Welding Process Analytics Database architecture specified in D5.2.

Under T9.2, the FOM was calibrated against bead-on-plate benchmark experiments using both dynamic observations (surface camera recordings of melt pool geometry and keyhole dynamics) and static cross-sectional and longitudinal sectioning. Calibration targeted elusive material properties near the boiling point (particularly the temperature- and composition-dependent surface tension) through systematic parameter identification. Identified limitations include material data uncertainty, spatial discretisation error, and beam shape frequency investigations, all of which will be addressed iteratively as experimental data from WP11-12 accumulates. A summary of the validation and additional simulation results for stainless steel is presented in a LANE 2026 paper [2].

Under T9.3, a comprehensive review of ROM architectures (fully data-driven methods, Physics-Informed Neural Networks, and intrusive projection-based approaches) was conducted against six requirements covering speed, accuracy, parameter coverage, data efficiency, integration, and extensibility. A fully data-driven, non-intrusive strategy was selected and implemented as a modular framework that supports different models, such as Gaussian Process Regression, Neural Networks, and Support Vector Regression, interchangeably. Early feasibility of this approach is demonstrated concretely by a LANE 2026 conference paper [3], accepted under the Lasers4MaaS grant acknowledgment, in which forward and inverse ML models trained on 73 Full-Order Model FOM simulations of 316L stainless steel achieve a median relative accuracy exceeding 97% on weld depth predictions, with full weld pool geometry inference completing within seconds.

2. Introduction

2.1. Background and Motivation

The manufacturing industry is currently experiencing a shift towards digital servitisation, driven by carbon-neutrality goals and rising demand for mass customisation. To enable the smart, decentralised, and sustainable factories of the future, the Lasers4MaaS project advances laser beam welding through a comprehensive "Laser-as-a-Service" digital platform. Central to this goal is the need for a reliable, high-precision, physics-based simulation system that can accurately predict and manage the complex interactions between laser and material.

Laser beam welding (LBW) is an inherently complex process characterised by nonlinear thermal and fluid dynamics. Traditional experimental optimisation is constrained by a "black-box" approach, which requires lengthy, costly iterative testing to identify suitable configurations [4]. This issue directly relates to Challenge C3 (controllability) mentioned in the proposal. The development of dynamic beam-shaping technologies, such as Coherent Beam Combining (CBC), introduces an almost endless variety of laser beam profiles, further complicating the problem by expanding the parameter space well beyond what can be explored experimentally within a reasonable timeframe [5] [6]. To manage this extensive configuration space, Lasers4MaaS depends on high-fidelity simulation models validated with experimental data [7].

These physics-based models provide validated synthetic data that support training Machine Learning (ML) models mentioned in WP7-8 and the development of computationally efficient Reduced-Order Models (ROMs) in WP10. Acting as a reliable baseline, calibrated Full-Order Models (FOM) eliminate the need for extensive physical re-testing for each new industrial scenario. Preliminary studies indicate that such ROMs can achieve median accuracies of up to 97% against synthetic data in predicting critical weld features [3]. By integrating fundamental physics with industrial applications, this high-fidelity approach ensures that laser welding can be performed with the flexibility and quality needed for a resilient EU manufacturing ecosystem. [8]

2.2. Scope of Deliverable

This deliverable establishes the core technical foundation for the predictive aspects of the Lasers4MaaS project. D9.1 focuses on developing, calibrating, and validating the FOM and reviewing suitable ROMs.

Specifically, this report covers:

- **Model Architecture (T9.1):** Implementation of a multiphase, compressible Mass of Fluid model [7], incorporating CBC laser representation [6].
- **KPI Extraction (T9.1):** Automated processes for exporting welding fingerprints, such as depth, width, and length, into interoperable formats for the project database.
- **Calibration and Validation (T9.2):** Aligning the FOM with experimental data to ensure the model serves as a trustworthy “ground truth."
- **ROM Strategy Selection (T9.3):** A comprehensive review of Reduced-Order Modelling architectures to identify the best strategy for real-time calculations, focusing on balancing computational speed and predictive accuracy.

This deliverable does not include the complete implementation, training, and tuning of the chosen ROM algorithms, nor does it cover the creation of the large-scale synthetic dataset for training WP7-8 algorithms. These tasks will be done in Deliverable D10.1.

2.3. Relation to Other Work Packages and Deliverables

Deliverable D9.1 is a vital step in the Lasers4MaaS process, ensuring that detailed physical models are converted into usable digital assets for the broader project. The table below highlights the main technical dependencies and points of integration.

Table 1: Presentation of connections to other parts of the Lasers4MaaS project.

Interdependency	**Reference**	**Contribution**
Inward Dependency	WP11, WP12	Providing experimental data.
Forward Integration	WP10 (D10.1)	Delivery of the validated model architecture along with the chosen ROM strategy.
Data Provisioning	WP7, WP8	Export of high-quality synthetic datasets for AI-based decision-making and control modules.
Interoperability	WP5, WP6 (D5.2)	Ensuring that simulation KPI outputs align with the overall project database architecture for smooth data integration.
Scientific Output	T9.3	Two publications for the 14th CIRP Conference on Photonic Technologies (LANE 2026).

3. High-Fidelity Physics-Based Simulation Model (T9.1)

3.1. Model Architecture and Governing Equations

Model Architecture

The fluid-dynamical partial differential equations are solved using a modified compressible version of OpenFOAM's *multiphaseInterFoam* solver. The numerical framework is based on the Mass-of-Fluid approach introduced by Zenz et al. [7]. The model describes a multiphase system consisting of solid metal, liquid metal, metal vapor, and ambient gas.

To distinguish between the original solid material and the material that has undergone melting, also a resolidified phase is introduced. This enables a clear visualization and analysis of the weld seam independently of the base material. The ambient gas phase can represent air or any shielding gas, thereby allowing the simulation setup to closely reproduce the experimental conditions. In addition, the model accounts for all relevant phase changes. Melting and solidification are modeled as temperature-dependent processes, whereas evaporation and condensation are pressure-dependent.

Compared to incompressible one-fluid approaches, the compressible multiphase formulation provides significant advantages. In these models, gaseous phases are commonly excluded from the computational domain and are represented only through boundary conditions. In contrast, the present approach explicitly resolves the gaseous phases. Consequently, the recoil pressure effect is generated naturally through the high pressure of the expanding vapor phase, eliminating the need for empirical calibration or phenomenological recoil pressure models [1].

Governing Equations

The continuity equation is given by:

$$\frac{\partial \rho_i}{\partial t} + \nabla \cdot (\rho_i \boldsymbol{u}) = \dot{\rho}_i$$

where $\boldsymbol{u}$ and ρ denote velocity and density, respectively. The source term on the right-hand side ensures the mass exchange between phases during phase change.

The Navier-Stokes equation (momentum equation) is expressed as:

$$\frac{\partial (\rho \boldsymbol{u})}{\partial t} + \nabla \cdot (\rho \boldsymbol{u}\boldsymbol{u}) = -\nabla p + \nabla \cdot \boldsymbol{\tau} - \boldsymbol{S}_B + \boldsymbol{S}_S + \boldsymbol{S}_D$$

where p and $\boldsymbol{\tau}$ denote pressure and viscous stress tensor, respectively. The source terms $\boldsymbol{S}_B$, $\boldsymbol{S}_S$, $\boldsymbol{S}_D$ denote gravity, surface tension, and solid movement restriction term, respectively.

The energy equation consists of the convective and the conductive part. The convective part of the energy equation is formulated as:

$$\frac{\partial H_i}{\partial t} + \nabla \cdot (H_i u) = Q_{abs,i} + \dot{H}_i$$

with the energy H and Q_{abs} absorbed laser energy. Analogous to the continuity equation, the source term on the right-hand side accounts for energy transfer during phase changes.

The conductive part of the energy equation is given by:

$$\frac{\partial(\rho c_p T)}{\partial t} = \nabla \cdot (\lambda \nabla T)$$

where T, c_p, and λ denote temperature, specific heat capacity, and thermal conductivity, respectively.

3.2. Extensions and updates to the existing model

Solid Movement Restriction

The solid movement restriction term was modeled according to the Carman-Kozeny equation [9]:

$$\boldsymbol{S}_D = -\frac{\mu}{A_{perm}} \frac{{\alpha_S}^2}{(1-\alpha_S)^3 + \delta} \boldsymbol{u}$$

where α_S and μ denote the solid volume fraction and the dynamic viscosity, respectively. A_{perm} stands for the permeability area of the mushy zone, while δ is a small constant to avoid division by zero in fully solid regions. The formulation produces no movement restriction in liquid and gaseous regions, while a strong damping effect in solid regions while maintaining a continuous transition within the mushy zone. Such a treatment enables thermal expansion of the solid material due to the temperature dependent density of the metal.

In addition, an alternative approach for suppressing solid movement was implemented. In this method, the momentum equation is solved without the previously discussed source term. Subsequently, the velocity field is corrected by enforcing zero velocity in the solid phase, accompanied by a corresponding pressure correction. One disadvantage of this method is that any force acting on the solid material leads to instability of the simulation. Therefore, the solid density must remain constant when this method is applied. However, the approach provides a valuable reference for comparison with the firstly introduced model.

Surface Tension Model

A new surface tension model was implemented to improve the prediction of melt pool behavior, particularly in the vicinity of the keyhole and along the weld surface. The revised formulation provides a more accurate representation of contact angles, which is essential for correctly reproducing surface structures and weld seam elevation.

Interface Sharpening

As with all high-fidelity simulations, numerical diffusion can lead to smeared phase interfaces. To mitigate this effect, interface compression techniques are employed to maintain sharp phase boundaries. Within the present work, the interface compression strength was systematically adjusted. This parameter is highly sensitive: insufficient compression leads to diffuse interfaces, whereas excessive compression may result in numerical instabilities. Furthermore, the necessity of interface compression between specific phase combinations was investigated in detail.

Dynamic Mesh Refinement

Dynamic mesh refinement was implemented using carefully selected refinement criteria. Fine mesh cells are applied in regions of particular interest, such as the laser material interaction zone, the keyhole, and the melt pool. In contrast, coarser mesh cells are employed in the resolidified region, in the ambient gas, and in solid regions where no phase changes occur. This strategy significantly improves computational efficiency while maintaining high local accuracy.

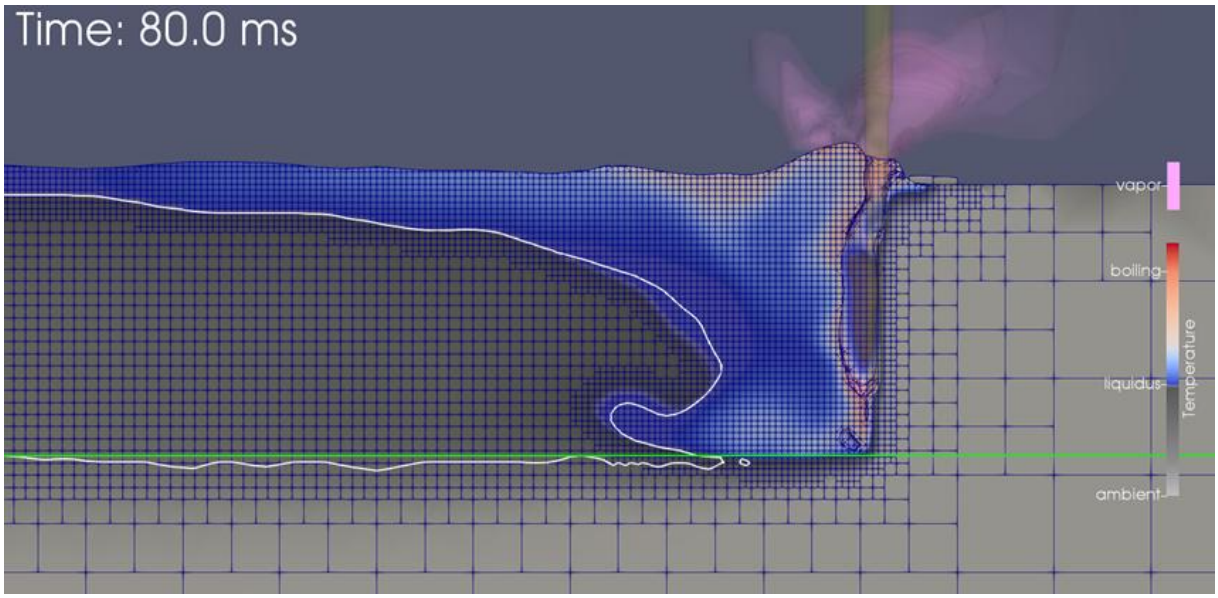

Figure 1: Dynamic mesh refinement used in the simulations with fine cells applied in the regions of interest

Parallelization Improvements

The numerical framework was further optimized to improve robustness and stability during parallel execution. These improvements enable simulations on a larger number of processor cores, thereby reducing computational time.

3.3. Laser Beam Representation

The laser beam is included in the model through Q_{abs} in the convective energy equation. At the current state, only solid and liquid phases absorb the laser energy, not the gaseous phases.

One characteristic of the coherent beam combining (CBC) laser technology is having both a spatial and a temporal intensity distribution. That means the laser source is described by a beam shape and its frequency. If assumed that the frequency is high enough to have an effect on the welding, only the spatial distribution is relevant and static beam shapes can be used in the simulations. Otherwise, the temporal intensity distribution should be also taken into account (dynamic beam shaping).

In the simulations, the beam shapes are interpolated on the numerical mesh and distributed between the cells according to the spatial intensity distribution. In case of dynamic beam shaping, another factor is the frequency of the beam shape. The separate single laser spots are activated successively for a time slot according to the frequency of the beam shape.

3.4. Material Modelling for Use Cases

Stainless Steel

The material model for stainless steel was developed for 316L stainless steel, as this alloy covers the majority of the investigated use cases, including food packaging, hydrogen power, fusion plant, and pharma. The thermophysical properties, including density, specific heat capacity, and thermal conductivity, were implemented as temperature-dependent functions according to Pichler et al. [10] [11]. Certain material properties remain difficult to determine experimentally, particularly close to the boiling temperature. Furthermore, the temperature dependence of the surface tension is strongly influenced by the sulfur content of the alloy. The calibration strategy employed to determine these uncertain but highly influential parameters is discussed in detail in Section 4.1.

Aluminium

For aluminium applications, the material model was developed for a 5xxx series aluminium alloy. Compared to 6xxx alloys, 5xxx alloys exhibit improved resistance to hot cracking, resulting in a better reproducibility in both experiments and simulations. The use cases covered by aluminium are the automotive and the aerospace applications. The thermophysical properties, including density, specific heat capacity, and thermal conductivity, were implemented as temperature-dependent functions according to Jiang et al. [12] and Leitner et al. [13]. As in the case of stainless steel, some material properties close to the boiling temperature are insufficiently accessible. In addition, the temperature dependence of the surface tension of aluminium is particularly sensitive to its oxygen content.

Solid Movement Restriction Parameters

A_{perm} is material-dependent and was therefore determined for the materials of the use cases. $A_{perm} = 10^{-13}$ m^2 was found for stainless steel, while $A_{perm} = 10^{-12}$ m^2 worked best for the aluminium alloy. For both materials, $\delta = 10^{-3}$ was an efficient choice.

4. Calibration and Validation (T9.2)

4.1. Calibration Strategy

The calibration of the numerical model involves several challenges, all of which require parameter identification for material properties that are difficult to determine experimentally but have a significant influence on the simulation results.

One major challenge arises from the fact that certain material properties cannot be measured directly, especially in temperature regions close to the boiling point. When material properties are unknown only in limited temperature ranges, the most straightforward initial approach is linear extrapolation from the experimentally accessible regime. In many cases, this provides a reasonable first approximation. If linear extrapolation proves insufficient, a more detailed investigation of the material's molecular behavior becomes necessary. For example, alloying elements may evaporate at different temperatures, leading to strongly nonlinear temperature dependencies of the material properties near the boiling point.

A second challenge originates from discrepancies between experimental data reported in the literature. Measurements performed by different laboratories frequently differ because of variations in laboratory environments, experimental setups, and measurement techniques. To address these uncertainties, the relevance of the individual measurement techniques was carefully evaluated with respect to the assumptions and physical processes represented in the simulations.

For all calibration steps, the assumed material behavior was implemented into the numerical model and compared with experiments. The convergence criteria included weld geometry, such as weld depth, weld width, and weld surface topology, as well as melt pool geometry, keyhole dynamics, and the occurrence of defects such as pores and spatters.

4.2. Benchmark Experiments

Benchmark experiments were conducted to calibrate and validate the physics-based numerical model. A primary objective was to ensure the highest possible consistency between experiments and simulations with respect to material, beam shape, surrounding gas, and laboratory conditions. All experiments were performed as bead-on-plate welding processes in order to simplify the geometry and minimize uncertainties associated with more complex joint configurations, e.g. gaps between plates.

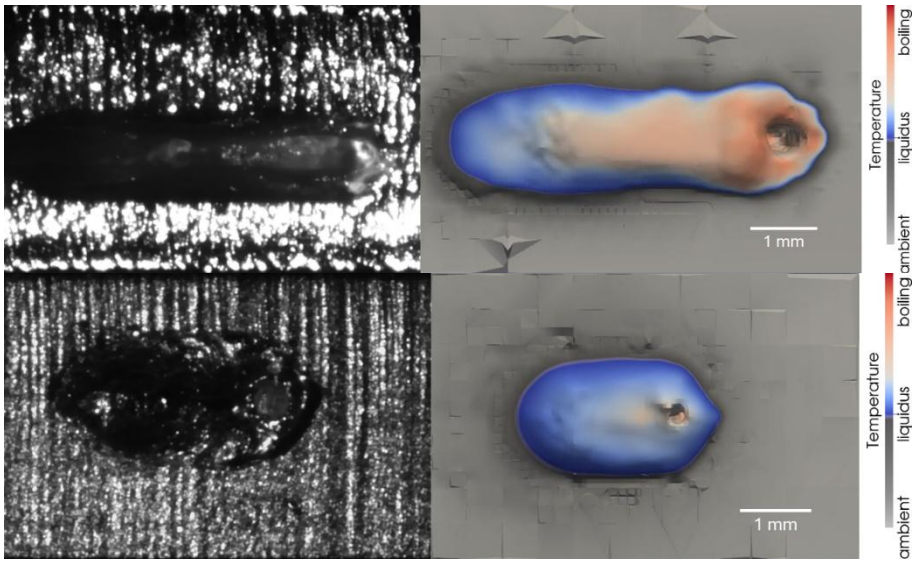

Figure 2: Surface camera images compared with simulations in stainless steel (top) and aluminium (bottom)

Dynamic measurements

Surface camera recordings were used to investigate the dynamic process behavior. These measurements provided information about melt pool length, width, melt pool surface flow, spatter formation, and keyhole dynamics. A major advantage of this approach is that it enables analysis not only of the final welding results but also of the transient process behavior. Figure 2 presents a comparison between experimentally recorded surface images and the corresponding simulation results for the investigated materials.

Static measurements

Cross and longitudinal sections of the weld seam were analyzed using established metallographic methods. These investigations provided information regarding penetration depth, weld bead geometry, and porosity. In addition, cooling and solidification directions could be inferred from the grain orientation. Representative cross and longitudinal sections are shown and discussed in detail in Section 4.3.

4.3. Validation Results

The simulations were validated against the experiments using the input parameters summarized in Table 2. For the sake of simplicity, the simulations were performed with static beam shapes. Consequently, a comparatively high beam shape frequency of 100 kHz was selected in the experiments to minimize the influence of the temporal discretization.

All simulations were performed using the same numerical framework and identical solver settings in order to ensure consistency throughout the validation study. The minimum mesh cell size applied in the simulations was 62.5 µm.

Table 2: Input parameters of the welding processes used for validation

Material	Beam Shape	Power [kW]	Feed Rate [m/s]
Stainless Steel (SS316L)	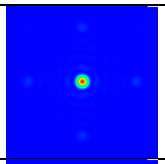	5	0.25
	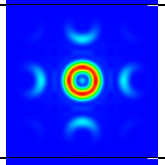	5	0.25
Aluminium (EN AW-5754)	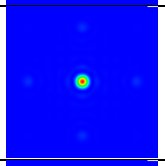	6	0.1
	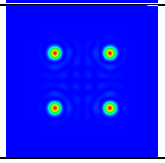	6	0.1

The primary basis for validation was the comparison between experimental and simulated cross-sections and longitudinal sections. The main evaluation criteria included weld seam geometry, weld depth, weld width, surface topology, and defect formation.

Stainless Steel

For stainless steel, the validation was performed using a single-spot and a circle beam shape. The cross-sectional comparisons are presented in Figure 3.

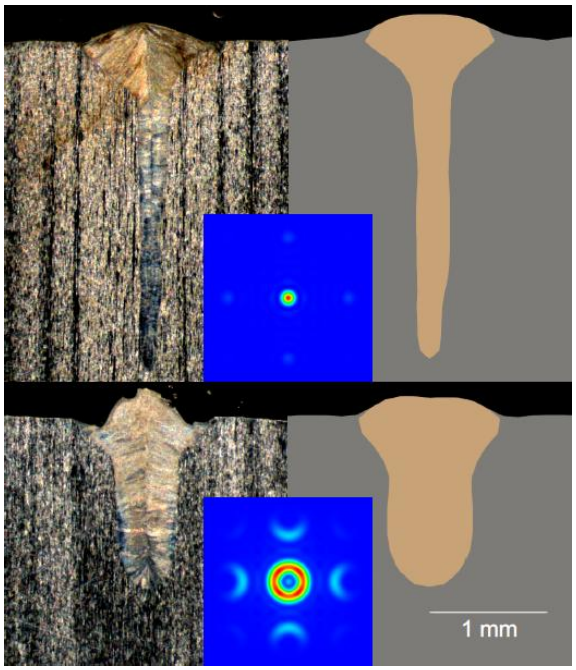

Figure 3: Cross section comparison of the welding of stainless steel at a power of 5 kW and a feed rate of 0.25 m/s with two different beam shapes. The scale applies for both the cross sections and the beam shapes. [2]

The comparison demonstrates that the numerical model successfully captures the influence of the beam shape on the resulting weld geometry. As expected, the larger circle beam shape produces a wider but shallower weld seam compared to the single-spot configuration. The single-spot case exhibits very good agreement between simulation and experiment in terms of penetration depth and weld width. For the circle beam shape, the simulation predicts a slightly wider cross-section and minor deviations in the weld surface topology. Nevertheless, the overall agreement remains satisfactory.

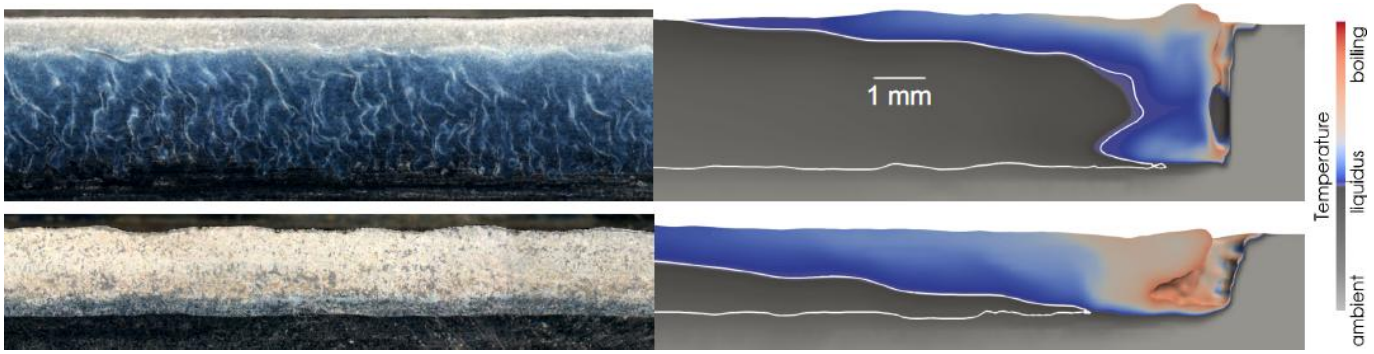

Figure 4: Long section comparison of the welding of stainless steel at a power of 5 kW and a feed rate of 0.25 m/s with two different beam shapes (top: single spot, bottom: circle). [2]

The longitudinal sections are shown in Figure 4. These provide additional insight into the physical mechanisms governing the welding process and further highlight the advantages of numerical simulations for process analysis. The investigated beam shapes produce different welding regimes, which consequently lead to distinct thermal histories and cooling conditions.

The experimentally observed color differences in the longitudinal sections indicate variations in the resulting metallurgical phases caused by different cooling rates. A more detailed explanation of the welding simulations of stainless steel can be found in the work by Vörös et al. [2].

Aluminium

For aluminium, the validation study was conducted using the single spot and a beam shape consisting of four spots. This beam shape was intentionally selected to evaluate the predictive capability of the model over a broader range of beam shapes. The cross-section comparison can be seen in Figure 5.

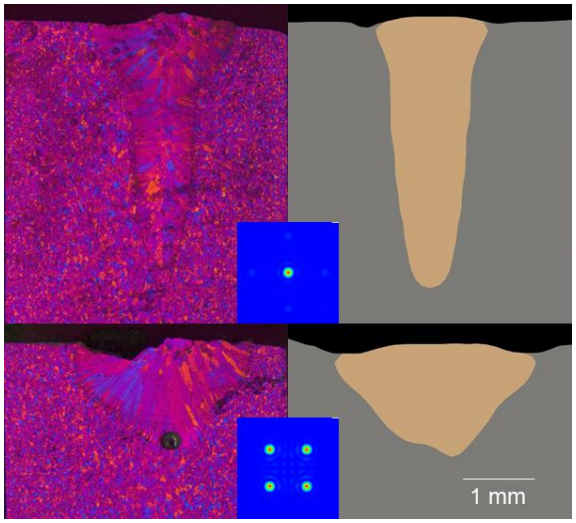

Figure 5: Cross section comparison of the welding of aluminium at a power of 6 kW and a feed rate of 0.1 m/s with two different beam shapes. The scale applies for both the cross sections and the beam shapes.

A direct comparison with the stainless-steel results reveals that the aluminium weld seams are significantly wider. This behavior is primarily attributed to the higher thermal conductivity of aluminium.

Similar to the stainless-steel simulations, the aluminium simulations show very good agreement with the experiments. The predicted weld geometries closely match the experimental cross-sections, with only minor deviations.

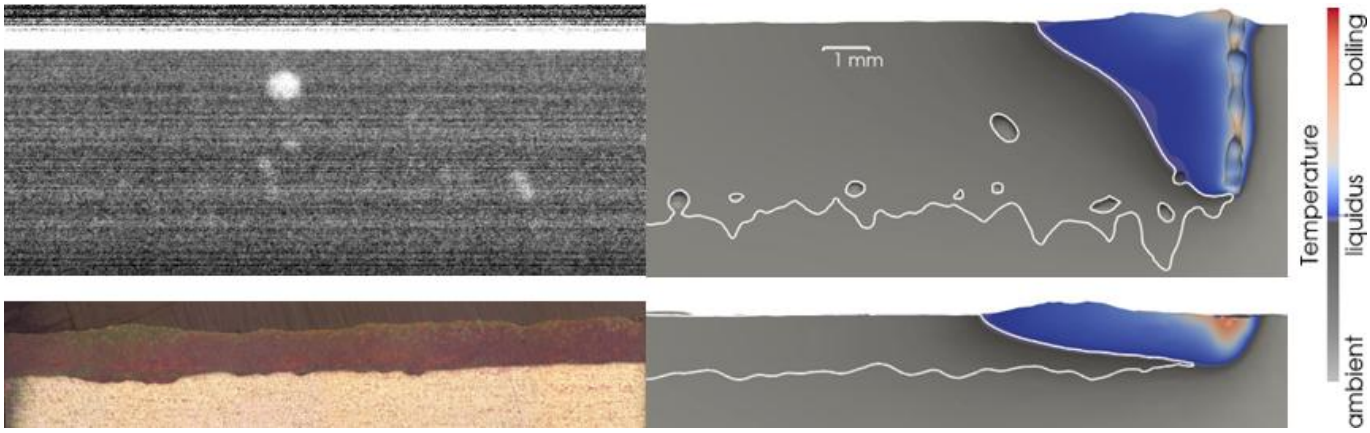

Figure 6: Long section comparison of the welding of aluminium at a power of 6 kW and a feed rate of 0.1 m/s with two different beam shapes (top: single spot, bottom: four spots).

Figure 6 shows the longitudinal sections. The single-spot configuration reveals the presence of porosity within the weld seam. Because of the wider weld seam in aluminium, pores cannot always be seen on a middle plain cut. Therefore, an X-ray image was used for comparison to reliably identify the porosity distribution.

The simulations were able to reproduce pore formation within the weld seam. Small pores were primarily predicted at the bottom, whereas fewer but larger pores appeared in the upper regions. The four-spot beam shape generated a shallower and longer melt pool. In this case, the predicted fluctuations in weld penetration depth showed promising agreement with the experiments.

4.4. Identified Limitations and Uncertainty Quantifications

Despite the overall good agreement between simulations and experiments, some limitations and uncertainties remain and should be addressed in future investigations.

One important uncertainty originates from the material data. Some material properties, particularly at temperatures close to boiling point, are not known with sufficient accuracy. Even small variations in these parameters may influence melt pool and keyhole geometry.

On the numerical side, spatial discretization must also be considered. Although a minimum mesh size of 62.5 µm provided stable and accurate results in the present work, a systematic study is still required to determine whether further refinement would significantly improve prediction accuracy. However, the mesh size should only be reduced further if the effect is significant, as this would increase the simulation time.

In addition, the influence of the beam shape frequency has not yet been investigated comprehensively. Since the present validation was performed with effectively static beam shapes, future work should analyze the influence of dynamic beam shaping on the welding process.

5. Reduced-Order Model Methodology Review and Selection (T9.3)

5.1. Requirements for ROMs Within Lasers4MaaS

The effectiveness of the ROMs in the Lasers4MaaS digital platform is essential for connecting high-fidelity physics simulations with real-time industrial use. To serve as a reliable basis for later review, these models will be vetted according to the following requirements:

- **Speed (R1):** To enable real-time AI-driven decision-making and process optimisation as outlined in WP7-8, ROMs need to deliver feedback almost instantly. The goal is to keep evaluation times under 5 seconds per iteration, which is crucial for closed-loop control and for quickly solving inverse problems in which process parameters are identified to meet target KPIs.

- **Accuracy (R2):** Precision is crucial for ensuring the reliability of the "physics-based digital twin." ROMs should aim for a relative error of no more than 10% relative to synthetic high-fidelity data outputs. This level of accuracy must be maintained while also providing a response time close to real time.

- **Parameter Coverage (R3):** The ROMs need to effectively manage the high-dimensional parameter space created by dynamic beam shaping. Additionally, the architecture should be easily extensible, enabling straightforward prediction of additional parameters.

- **Data Efficiency (R4):** Since FOMs are computationally expensive, requiring around 700 CPU-core-hours per simulation, ROM generation should be efficient, requiring only a minimal number of FOM simulations.

- **Integration (R5):** Outputs need to be in a standard, interoperable format (such as CSV or JSON) that can be directly used by the WP7-8 ML/AI training pipelines and the broader "Welding Process Analytics Database."

- **Extensibility (R6):** The methodology should be designed to facilitate model transferability, enabling it to generalise to new materials and beam configurations without requiring a full reimplementation.

5.2. Review and Assessment of ROM Approaches

To meet the ambitious objectives of the Lasers4MaaS project, high-fidelity physics-based digital twins need to be supported by computationally efficient Reduced-Order Models (ROMs) that enable real-time process control and quick inverse optimisation. We chose the ROM against the six previously discussed requirements.

Fully Data-Driven Approaches

Non-intrusive methods treat the high-fidelity solver as a "black box," focusing on directly mapping input parameters to welding results using synthetic datasets. Since these models can produce results nearly in real time, they meet the speed requirement (R1). Additionally, all these models can easily adapt to high-dimensional parameters and be implemented across various configurations, satisfying R3 and R6. Moreover, they provide outputs in a practical format, fulfilling R5. They are also data-efficient and meet R4, but since they are all data-driven, they generally need more data, as they depend heavily on it. Furthermore, preliminary studies, as discussed later, have shown that all of those methods can achieve the target accuracy of 10% (R2). In the following, we present three examples of fully data-driven methods:

- **Gaussian Process Regression (GPR):** GPR is an effective interpolator, especially beneficial for small datasets [14], making it ideal for laser welding where high-fidelity simulations are costly (e.g., 700 CPU-core-hours per run). Its key benefit is that it provides uncertainty estimates, making it a very powerful predictive tool.

- **Neural Networks (NN):** Such methods typically require larger datasets to generalise well and do not provide uncertainty estimates out of the box. However, it can be shown that they also meet the requirements of Lasers4MaaS.

- **Support Vector Regression (SVR):** SVR is known for its robustness and ability to handle high-dimensional spaces [15]. While it offers rapid training and inference, it lacks the probabilistic output of GPR and the flexibility of deep learning architectures, often making it less interpretable in a physical context

Besides those three methods, there are also numerous other methods which perform similarly. Such methods, as well as hybrid approaches with PINN, can also be combined with explainable AI techniques such as Shapley Additive Explanations (SHAP) analysis to interpret model predictions, as demonstrated by Meng et al. [16] in the context of laser beam welding.

Hybrid Approaches

In addition to fully data-driven techniques, hybrid methods such as Physics-Informed Neural Networks (PINNs) are also worth exploring [17] and an example can be found in the work of Meng et al. [16], who demonstrate a PIDL framework for porosity prediction in laser beam welding of aluminium alloys, achieving a 41% reduction in MSE over a conventional data-driven model. These approaches combine data-driven modelling with fundamental physical laws by incorporating governing equations into the training process, for example, either via the loss function or the model architecture [17]. This integration encourages predictions that are physically consistent and can greatly decrease the need for extensive synthetic datasets, improving both accuracy (R2) and data efficiency (R4). Similar to purely data-driven models, PINNs offer fast inference once trained, thus satisfying the speed requirement (R1). Furthermore, when properly designed, they can handle high-dimensional parameter spaces effectively, making them suitable candidates in terms of parameter coverage (R3).

However, these advantages come with notable trade-offs. Unlike fully non-intrusive approaches, PINNs typically require problem-specific formulation. The inclusion of additional physical variables or changes in governing equations often necessitates modifications to the model structure or loss formulation. This

reduces their flexibility and makes them less straightforward to extend to new materials or beam configurations, posing challenges for extensibility (R6) and, to some extent, parameter scalability (R3).

Physics-Based Approaches

Intrusive methods project the governing equations of the full-order model (FOM) onto a reduced subspace, preserving physical consistency but requiring modifications to the direct solver. A primary example is the Galerkin projection combined with Proper Orthogonal Decomposition (POD), in which a reduced basis is constructed from high-fidelity simulation snapshots [18]. This enables very rapid evaluations (R1), although the inference phase still requires more computation than data-driven approaches. POD can attain high accuracy (R2) within the parameter space defined by the snapshots and, because the physics are explicitly preserved, it does not require large datasets beyond basis creation.

However, these methods demand considerable customisation (R6). The intricacy of the FOM, involving multiple coupled equations and numerical algorithms, complicates implementation and restricts scalability across wider parameter spaces (R3). Extending the model generally requires extra development time, though it can be integrated into standard workflows (R5) once in place.

Initial tests indicated that POD-Galerkin effectively models heat conduction in simplified scenarios. However, extending it to the complete solver or integrating it with data-driven elements proved challenging. In brief, intrusive methods provide robust physical accuracy and quick computation but are hampered by high implementation complexity and lower adaptability in complex situations.

5.3. Selected ROM Strategy and Justification

Based on the requirements in Section 5.1 and the assessment in Section 5.2, a fully data-driven, non-intrusive strategy has been chosen as the ROM architecture for WP10. This decision is mainly driven by its strong balance across all six criteria: real-time inference speed (R1), accuracy comfortably within the 10% target (R2), ease of extension to new materials and beam setups (R3, R6), data efficiency considering the high costs of FOM runs (R4), and seamless integration with the project's interoperable data pipeline (R5).

A key insight from the initial studies in Section 5.4 reveals that different model architectures excel in predicting different output quantities. For example, GPR is most effective for weld depth, whereas NNs are more effective at predicting length. Instead of choosing a single model prematurely, the strategy employs a flexible, modular architecture that supports GPR, NN, SVR, and other data-driven methods within the same framework. This approach enables the selection of the most suitable model for each specific case as the larger synthetic dataset is developed in WP10, without requiring structural changes to the existing infrastructure.

This methodology can also be considered physics-informed machine learning with observational bias, because the training data comes solely from a validated, physics-based FOM rather than arbitrary empirical sources [19]. This offers an implicit physical basis without the formulation complexity of intrusive PINN methods, as previously discussed.

5.4. Preliminary Evidence

To provide concrete, early evidence for the selected ROM strategy, a machine-learning study was conducted using a synthetic dataset generated from the validated FOM described in Sections 3 and 4. This work has been accepted to the 14th CIRP Conference on Photonic Technologies (LANE 2026) under the Lasers4MaaS grant acknowledgement and constitutes the primary scientific output of T9.3 [3].

The study investigated laser beam welding of 316L stainless steel, used in UC2 and UC4. Furthermore, UC5 uses ferritic stainless steel, which is closely related as well. The input parameters included laser power (4000–8000 W), welding speed (0.20–0.40 m/s), and beam-shape radius, as shown in Figure 7, which together covered 17 different CBC profiles. A total of 73 high-fidelity FOM simulations were performed using a Sobol-based space-filling sampling method combined with manually chosen sampling points of special interest. On average, one simulation consumed about 700 CPU-core-hours, highlighting the importance of efficient ROMs for feasible parameter studies.

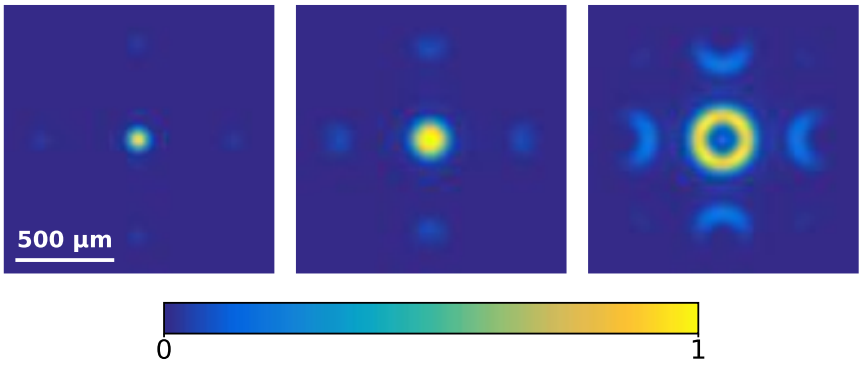

Figure 7: Examples of normalised intensity distributions of the used beam shapes. To the left is a circle with radius 0 (single spot). The middle and right figures depict circles with radii of 8 (medium circle) and 16 (large circle), respectively.

The forward problem, predicting weld pool geometry from three input parameters, was tackled using GPR, NN, and SVR, evaluated through two separate 10-fold cross-validations. All three techniques showed strong predictive accuracy. For weld depth, both GPR and NN achieved a median relative accuracy over 97% on the synthetic dataset, meeting the 10% error threshold (R2). In predicting weld length, the NN performed best, whereas GPR slightly outperformed for width. All results across different metrics are shown in Figure 8. Notably, inference for any single parameter set is completed within seconds, meeting the real-time speed requirement (R1).

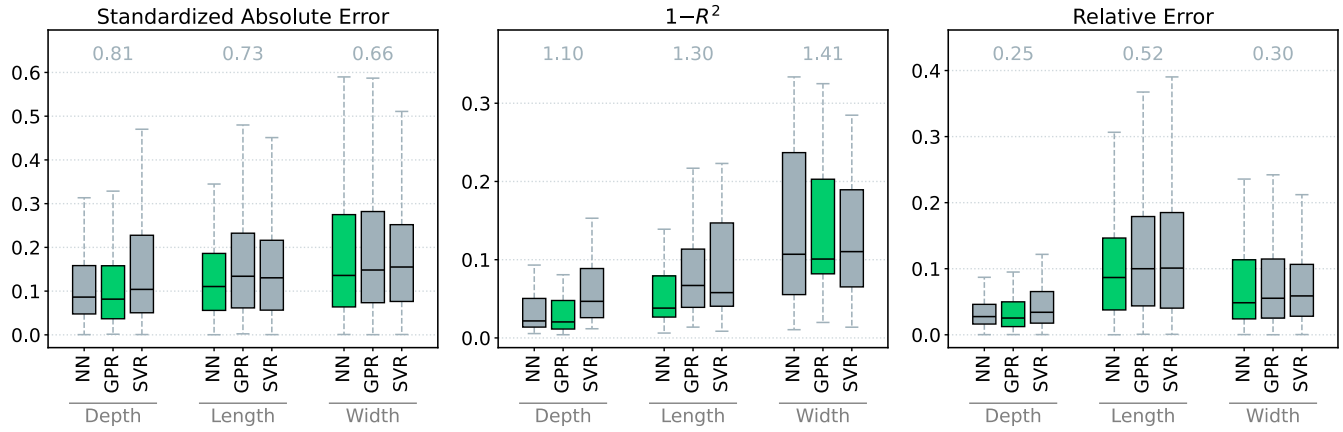

Figure 8: Evaluation of predictions in the forward direction. The comparison includes a Neural Network (NN), Gaussian Process Regression (GPR), and Support Vector Regression (SVR) for predicting maximum depth, length (at 50% depth), and width (at 50% depth and 50% length) from the three input parameters (power, velocity, and beam shape radius). Panels show standardised absolute error, residual variance ($1-R^2$), and relative error. Green boxes highlight the best-performing method per category. Top numerical values indicate baseline performance when always predicting the median value.

Additionally, a convergence study shown in Figure 9, indicated GPR provides reliable depth predictions with as few as 30 training samples, underscoring its data efficiency (R4) and suggesting the dataset can grow incrementally as more FOM simulations are completed in WP10.

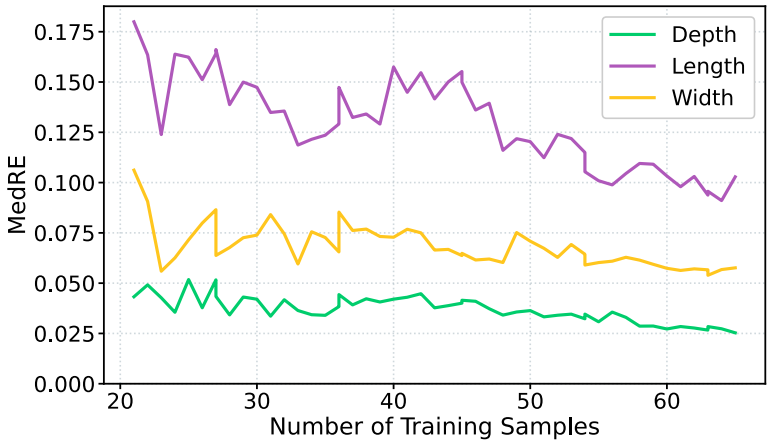

Figure 9: Evolution of the Median Relative Error (MedRE) with sample size when predicting output parameters using Gaussian Process Regression.

Beyond point predictions, the forward models enable rapid reconstruction of the full weld pool geometry for arbitrary parameter combinations within the search space, including longitudinal (Figure 10) and transverse cross-sectional profiles. This provides welding engineers with an intuitive visualisation tool to assess process outcomes before committing to physical trials.

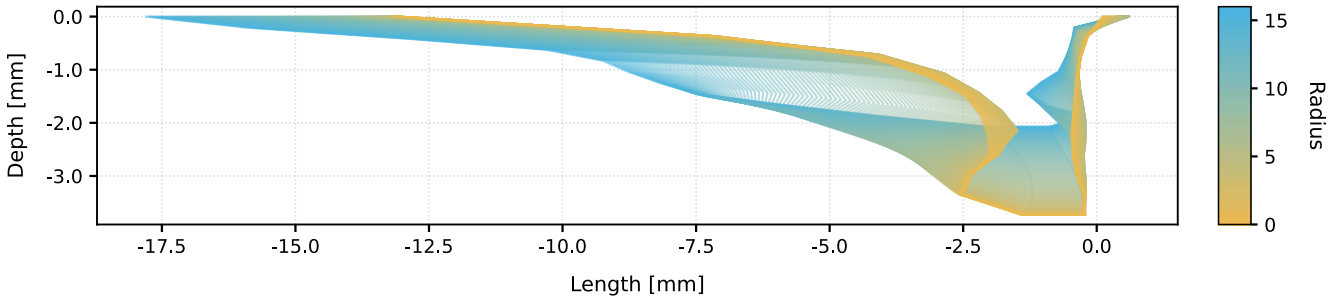

Figure 10: Longitudinal section of the weld pool for different shape radii as produced by the Neural Network approach.

For the inverse problem of determining input parameters that achieve a specific weld depth, a loss-surface approach, as depicted in Figure 11, was used with the GPR forward model. This is because a naïve prediction cannot be used as the forward mapping is non-injective; multiple input combinations can produce the same depth target. Instead of viewing this as a limitation, the method takes advantage of it: dense Sobol sampling covers the entire parameter space using the forward model, valid solutions are found within a tolerance set around the optimum, and a diverse subset is chosen by maximising mutual distance in solution space. This process completes in seconds and can be enhanced with restarted Bayesian optimisation to find the globally optimal configuration, such as the one with the lowest energy input. The accuracy of inverse predictions is directly linked to the forward model's performance, which is approximately 97% for weld depth relative to the synthetic baseline.

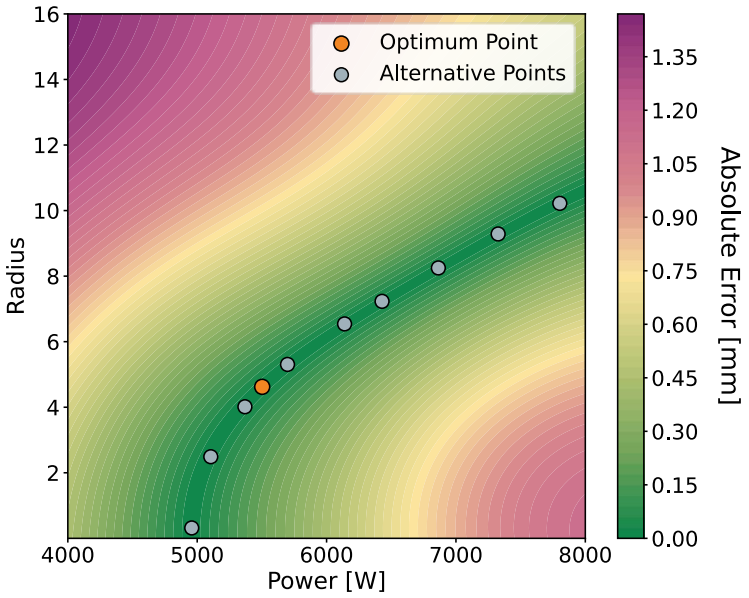

Figure 11: Two-dimensional loss surface as created by the forward model for a target depth of 3 mm. While the laser power and the shape radius were varied, the welding speed was fixed at 0.25 m/s.

Taken together, these results provide compelling early evidence that the selected data-driven ROM architecture is both feasible and well-suited for integration into the Lasers4MaaS digital platform as the process selector and process optimiser services described in WP7-8.

6. Interoperability of the High-Fidelity Simulations

Since the high-fidelity simulations are based on physical models, they allow the identification of mechanisms that influence the welding process. One major benefit is the possibility to investigate the process with very high temporal and spatial resolution. This enables a deeper understanding of the underlying mechanisms, supports process control and development, and facilitates the extraction of quantitative data for identifying correlations between variables, e.g. between laser power and temperature distribution.

The interoperability between high-fidelity simulations and experiments is of particular importance. Such comparisons are essential for the validation of the simulation model (Section 4.3), and support the improvement of both the experimental setup and the simulation methodology. The interoperability was achieved through the use of the Visualization Toolkit (VTK) data format. The VTK format enables efficient extraction, sharing, and analysis of simulation data, which can subsequently be compared with experimental measurements. Additional details regarding the advantages of the VTK format and its integration into the project workflow are discussed in detail in D11.1.

Error! Reference source not found. shows an example, where simulations were performed with an applied power modulation. From these simulations, temperature and velocity fields were extracted on a regular numerical grid. The datasets included spatial coordinates (x, y, z), time (t), temperature (T), and velocity (U). The simulation results can be directly compared with data acquired from sensors and camera systems of the experiments.

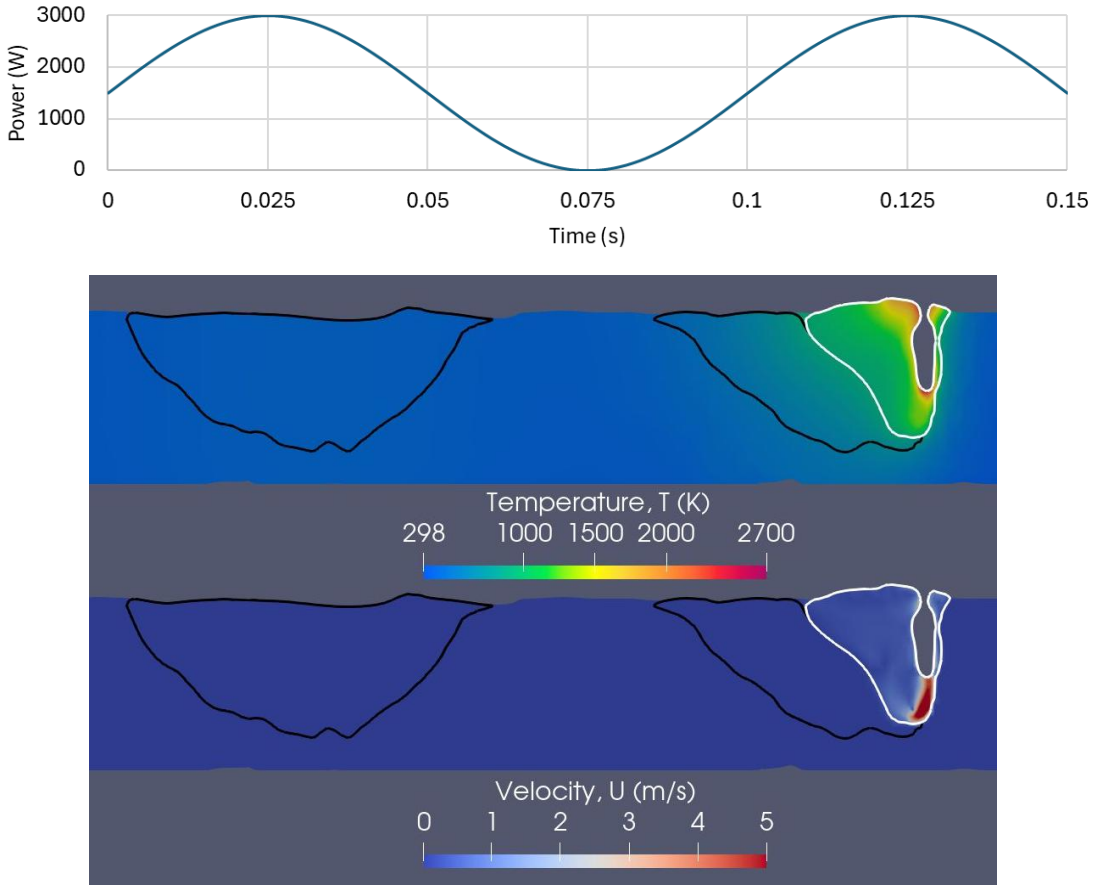

Figure 12: Power modulation and the corresponding long sections of welding simulations showing temperature and velocity fields. White color indicates the melt pool, black color indicates the resolidified material.

7. Contribution to Project KPIs and Expected Outcomes

The outputs of D9.1 most directly target two key PREDICT KPIs. For process fidelity computation time, the goal is to reduce simulation time from 700 CPU-core-hours per FOM to nearly instantaneous predictions using ML-based ROM inference for single features. The combination of the validated FOM and the data-driven ROM architecture outlined in Section 5.3 provides a complete technical pathway to achieve this, with the results from the LANE 2026 publication [3] results already demonstrating that full weld-pool geometry predictions can be made within seconds. Regarding FOM-versus-ROM accuracy, the aim is to match the FOM's own error rate of below 10%. Initial results surpass this goal, with both GPR and NN models achieving median accuracy exceeding 97% on weld depth compared to the synthetic baseline.

These accomplishments provide immediate cascading advantages across other pillars. Rapid ROM inference supports the process optimisation KPI by enabling quick, reduced-order parameter sweeps across the entire beam shape space, making them computationally efficient. For the IMPROVE goals, physics-based simulation outcomes serve as a solid pre-trained baseline for AI models, ensuring their predictions are grounded in validated physical principles from the outset.

On the connectivity side, all simulation KPI outputs can be easily exported in JSON and CSV formats, with field naming aligned with the Welding Process Analytics Database architecture specified in D5.2, directly supporting the CONNECT interoperability objectives and ensuring seamless ingestion by downstream WP5-6 and WP7-8 modules.

D9.1 thereby delivers all outputs contractually required under T9.1, T9.2, and T9.3 of the Description of Action, in full alignment with the project's M18 milestone obligations.

8. Summary and Conclusion

Task T9.1 delivered a compressible multiphase Mass-of-Fluid Full-Order Model implemented within a modified OpenFOAM solver, resolving the coupled thermal, fluid-dynamical, and phase-change phenomena of laser beam welding across four distinct phases: solid metal, liquid metal, metal vapor, and ambient gas. The model covers two material systems:

- stainless steel for use cases UC2, UC3, and UC5,
- aluminium for UC1 and UC4

The Model also incorporates static and dynamic laser representations suitable to simulate welding with CBC. Its defining technical innovation is the physically self-consistent generation of the recoil pressure effect through the natural pressure build-up of the expanding vapor phase, making empirical recoil pressure coefficients unnecessary and removing an entire class of calibration uncertainty present in conventional one-fluid approaches. Extensions implemented during this reporting period include an improved surface tension model, interface compression tuning, dynamic mesh refinement, and parallelisation improvements.

Task T9.2 established the calibration strategy and benchmark experimental infrastructure against which the FOM is validated. Bead-on-plate experiments using both dynamic surface camera observation and static cross-sectional and longitudinal sectioning were conducted under controlled conditions for 316L stainless steel and an aluminum alloy. The calibration procedure targeted elusive material properties like the temperature-dependent surface tension, which varies strongly with sulfur content in steel and oxygen content in aluminium.

Task T9.3 selected a fully data-driven, non-intrusive ROM architecture, implemented as a modular framework supporting among others Gaussian Process Regression, Neural Networks, and Support Vector Regression. Evidence for this is the LANE 2026 conference paper [5], accepted under the Lasers4MaaS grant acknowledgement, which demonstrates that GPR and NN models trained on 73 high-fidelity FOM simulations of 316L stainless steel achieve median relative accuracy exceeding 97% on weld depth, with full weld pool geometry predictions completing within seconds. This modular strategy feeds directly into WP10, where the framework will be trained on the large-scale synthetic dataset generated by the FOM, and into WP7-8, where ROM inference will serve as the computational backbone of the process selector and process optimiser services.

Taken together, the simulation infrastructure established in D9.1 provides the validated physical foundation from which Lasers4MaaS will build its physics-informed AI ecosystem, accelerating the transition from smart, decentralised factories to interconnected smart value networks.

9. Bibliography

[1] C. Zenz, P. S. Cook, L. Vörös and A. Otto, "A Critical Comparison of One- and Two-Fluid Approaches for the Simulation of Laser-Induced Melt Pool Formation and Vaporisation," *Discover Materials,* vol. 5, no. 1, p. 266, 2025.

[2] L. Vörös, J. D. Neuhauser, T. Florian, C. Zenz and A. Otto, "Numerical Investigation of Keyhole and Melt Pool Stability in Laser Welding of Stainless Steel," in *14th CIRP Conference on Photonic Technologies*, 2026.

[3] J. D. Neuhauser, L. Vörös, T. Florian, C. Zenz and A. Otto, "Forward Thinking, Inverse Solving: Data-Driven Weld Pool Prediction from CFD-Simulated Laser Beam Welding," in *14th CIRP Conference on Photonic Technologies*, 2026.

[4] J. Wu, C. Zhang, K. Lian, J. Sun and S. Zhang, "Processing Parameter Optimization of Fiber Laser Beam Welding Using an Ensemble of Metamodels and MOABC," *Frontiers of Mechanical Engineering,* p. 47, 2022.

[5] J. Wagner, A. Heider, R. Ramsayer, R. Weber, F. Faure, A. Leis, N. Armon, R. Susid, O. Tsiony, E. Shekel and T. Graf, "Influence of Dynamic Beam Shaping on the Geometry of the Keyhole During Laser Beam Welding," *Procedia CIRP,* vol. 111, pp. 448-452, 2022.

[6] R. Weber, J. Wagner, C. Hagenlocher, A. Spira, B. Urbach, E. Shekel and Y. Vidne, "Basic Properties of High-Dynamic Beam Shaping with Coherent Combining of High-Power Laser Beams for Materials Processing," *Journal of Manufacturing and Materials Processing,* vol. 9, no. 3, p. 85, 2025.

[7] C. Zenz, M. Buttazzoni, T. Florian, K. Crespo Armijos, R. Gómez Vázquez, G. Liedl and A. Otto, "A Compressible Multiphase Mass-of-Fluid Model for the Simulation of Laser-Based Manufacturing Processes," *Computers & Fluids,* vol. 268, p. 106109, 2024.

[8] T. Florian, K. Schricker, C. Zenz, A. Otto, L. Schmidt, C. Diegel, H. Friedmann, M. Seibold, P. Hellwig, F. Fröhlich, F. Nagel, P. Kallage, M. Buttazzoni, A. Rack, H. Requardt, Y. Chen and J. P. Bergmann, "Combining In Situ Synchrotron X-Ray Imaging and Multiphysics Simulation to Reveal Pore Formation Dynamics in Laser Welding of Copper," *International Journal of Machine Tools and Manufacture,* vol. 204, p. 104224, 2025.

[9] F. Rösler and D. Brüggemann, "Shell-and-tube type latent heat thermal energy storage: numerical analysis and comparison with experiments," *Heat and Mass Transfer,* vol. 47, pp. 1027-1033, 2011.

[10] P. Pichler, J. W. Sowards, B. J. Simonds and G. Pottlacher, "Measurements of thermophysical properties of solid and liquid NIST SRM 316L stainless steel," *Metals & corrosion,* vol. 55, pp. 4081-4093, 2020.

[11] P. Pichler, T. Leitner and E. Kaschnitz, "Surface Tension and Thermal Conductivity of NIST SRM 1155a (AISI 316L Stainless Steel)," *International Journal of Thermophysics ,* vol. 43, p. 66, 2022.

[12] Z. Jiang, X. Hua, L. Huang, D. Wu and F. Li, "Effect of multiple thermal cycles on metallurgical and mechanical properties during multi-pass gas metal arc welding of Al 5083 alloy," *Int J Adv Manuf Technol ,* vol. 93, p. 3799–3811, 2017.

[13] M. Leitner, T. Leitner, A. Schmon, K. Aziz and G. Pottlacher, "Thermophysical Properties of Liquid Aluminum," *Metallurgical and Materials Transactions A,* 2017.

[14] C. E. Rasmussen and K. I. Williams, Gaussian Processes for Machine Learning, MIT Press, 2006.

[15] A. J. Smola and B. Schölkopf, "A tutorial on support vector regression," *Statistics and Computing,* vol. 14, p. 199–222, 2004.

[16] X. Meng, M. Bachmann, F. Yang and M. Rethmeier, "Toward Prediction and Insight of Porosity Formation in Laser Welding: A Physics-Informed Deep Learning Framework," *Acta Materialia,* vol. 286, p. 120740, 2025.

[17] G. E. Karniadakis, I. G. Kevrekidis, L. Lu, P. Perdikaris, S. Wang and L. Yang, "Physics-Informed Machine Learning," *Nature Reviews Physics,* vol. 3, no. 6, pp. 422-440, 2021.

[18] P. Benner, S. Gugercin and K. Willcox, "A Survey of Projection-Based Model Reduction Methods for Parametric Dynamical Systems," *SIAM REVIEW ,* vol. 57, no. 4, p. 483–531, 2015.

[19] G. E. Karniadakis, I. G. Kevrekidis, L. Lu, P. Perdikaris, S. Wang and L. Yang, "Physics-Informed Machine Learning," *Nature Reviews Physics,* vol. 3, no. 6, pp. 422-440, 2021.